J. Fluid Mech. (2017), *vol.* 825, *pp.* 167–188. © Cambridge University Press 2017
doi:10.1017/jfm.2017.384

Vortical structures in the near wake of tabs with various geometries

A. M. Hamed[1], A. Pagan-Vazquez[1], D. Khovalyg[1], Z. Zhang[1] and L. P. Chamorro[1,2,3,†]

[1]Mechanical Science and Engineering Department, University of Illinois, Urbana, IL 61801, USA

[2]Civil and Environmental Engineering Department, University of Illinois, Urbana, IL 61801, USA

[3]Aerospace Engineering Department, University of Illinois, Urbana, IL, 61801, USA

(Received 10 October 2016; revised 23 May 2017; accepted 29 May 2017;
first published online 20 July 2017)

The vortical structures and turbulence statistics in the near wake of rectangular, trapezoidal, triangular and ellipsoidal tabs were experimentally studied in a refractive-index-matching channel. The tabs share the same bulk dimensions, including a 17 mm height, a 28 mm base width and a 24.5° inclination angle. Measurements were performed at two Reynolds numbers based on the tab height, $Re_h \simeq 2000$ (laminar incoming flow) and 13 000 (turbulent incoming flow). Three-dimensional, three-component particle image velocimetry (PIV) was used to study the mean flow distribution and dominant large-scale vortices, while complementary high-spatial-resolution planar PIV measurements were used to quantify high-order statistics. Instantaneous three-dimensional fields revealed the coexistence of a coherent counter-rotating vortex pair (CVP) and hairpin structures. The CVP and hairpin vortices (the primary structures) exhibit distinctive characteristics and strength across Re_h and tab geometries. The CVP is coherently present in the mean flow field and grows in strength over a significantly longer distance at the low Re_h due to the lower turbulence levels and the delayed shedding of the hairpin vortices. These features at the low Re_h are associated with the presence of Kelvin–Helmholtz instability that develops over three tab heights downstream of the trailing edge. Moreover, a secondary CVP with an opposite sense of rotation resides below the primary one for the four tabs at the low Re_h. The interaction between the hairpin structures and the primary CVP is experimentally measured in three dimensions and shows complex coexistence. Although the CVP undergoes deformation and splitting at times, it maintains its presence and leads to significant mean spanwise and wall-normal flows.

Key words: vortex flows, vortex interactions, wakes

1. Introduction

Static tabs of various shapes, inclination angles and orientations are often used as a passive control strategy to promote mixing and convective heat transfer (Stephens & Collins 1955; Zaman, Reeder & Samimy 1994; Gad-elhak 2000; Habchi *et al.* 2010*a*,*b*; Kaci *et al.* 2010; Ghanem *et al.* 2013). Turbulent transport past tabs is

† Email address for correspondence: lpchamo@illinois.edu

enhanced by the formation of energetic and long-lasting vortical structures such as hairpin-like vortices and a streamwise counter-rotating vortex pair (CVP) (Gretta & Smith 1993; Yang, Meng & Sheng 2001; Ghanem *et al.* 2012). Multiple studies have investigated the complex vortex dynamics in tab wakes; Gretta & Smith (1993), for example, used flow visualization and anemometry to characterize the flow past a trapezoidal tab. They proposed that a streamwise counter-rotating vortex pair is present in the wake and is enveloped by hairpin vortices along its length. In this phenomenological model, the two vortical structures coexist. Using planar laser-induced fluorescence (PLIF), Elavarasan & Meng (2000) found that the CVP and hairpin vortices dominate different regions of the wake. The CVP is dominant in a streamwise distance of $\sim 1.5h$ behind the tab, where h denotes the tab height. Beyond that location, hairpin vortices dominate the wake dynamics. Two later studies by Yang *et al.* (2001) and Dong & Meng (2004) supported the findings of Elavarasan & Meng (2000).

Planar particle image velocimetry (PIV) measurements by Yang *et al.* (2001) and direct numerical simulations (DNS) by Dong & Meng (2004) characterized the dynamics of the CVP and the hairpin vortices in the wake of trapezoidal tabs. These studies suggested the evolvement of the CVP into the hairpin vortex legs through a process of deformation and splitting. The head of the hairpin is rolled from a shear layer that forms near the top of the tab. Yang *et al.* (2001) found that the hairpin vortices are long-lasting structures persisting $\sim 12h$ downstream of the tab. Dong & Meng (2004) highlighted the role of hairpin vortices in mixing enhancement through the pumping of near-wall low-speed fluid into the outer flow. Furthermore, they found that the pairing and coalescence of hairpin vortices leads to vertical growth of the wake and increased mixing. Near the tab, the CVP plays a significant role in mixing through the common-up pumping at the central region of the wake. In contrast to the model of the CVP evolution into the legs of hairpin vortices, Habchi *et al.* (2010*b*), using a combination of laser Doppler velocimetry measurements and numerical simulations, found the CVP to retain coherence for $\sim 10h$ downstream of a trapezoidal tab; however, the CVP undergoes an exponential decay in strength. Very recent smoke visualizations by Park *et al.* (2016) have provided evidence for Kelvin–Helmholtz (KH) instability in the near wake at a Reynolds number $Re \sim 2000$ based on the hydraulic diameter of their test section. Further quantification of this instability and its effect on the mean flow and vortex dynamics remains to be addressed.

The complexity of the vortex dynamics in the tab wake is further dissected in the work of Dong & Meng (2004). The CVP and the hairpin vortices are classified as primary structures, as they are formed directly by the interaction between the tab and the surrounding flow. Secondary structures are also present in the wake; these are formed by the interaction of the primary vortices. A secondary hairpin vortex with the same sense of rotation as the primary one was observed by both Yang *et al.* (2001) and Dong & Meng (2004); the latter proposed that it originates from the wall-induced vorticity that is pumped by the primary hairpin vortex. Yang *et al.* (2001) observed another secondary vortical structure with a rotation opposite to the hairpin vortices; the three-dimensionality of this structure was challenging to map with planar PIV. Finally, a secondary streamwise CVP was identified by Dong & Meng (2004). This secondary CVP has an opposite sense of rotation to that of the primary one, making it disadvantageous to mixing, as it results in a downward flow at the central plane of the wake.

Trapezoidal tabs have received special attention due to their ability to generate hairpin vortices and their use in high-efficiency vortab (HEV) mixers. Tabs of

rectangular and triangular shapes are also used for control and mixing enhancement (Reeder & Samimy 1996; Chua, Yu & Wang 2003; Yu, Zhang & Shan 2015). Gretta (1990) suggested that the lack of a top flat edge in a triangular tab leads to the formation of a CVP but no hairpin vortices. Furthermore, Gretta (1990) reached the conclusion that trapezoidal tabs are better mixers through observation of the disturbance in a uniform hydrogen bubble sheet used for visualization. He noted that trapezoidal tabs had the maximum disturbance height caused by vortical structures. This finding led many of the following studies to focus on trapezoidal tabs. Furthermore, experimental efforts have mostly relied on flow visualization and planar PIV measurements, both of which have limited ability to characterize coherent three-dimensional (3D) structures such as hairpin vortices. While the DNS study of Dong & Meng (2004) provides a detailed description of the vortex dynamics within the wake, it was performed at a relatively low Reynolds number $Re_h \sim 600$ based on the tab height and free-stream incoming velocity.

The vortical structures in the wake of a similar element, a micro-ramp, have been frequently studied for use as a passive mechanism to control flow separation. The large-scale vortices in the wake of a micro-ramp exhibit similar organization to those in the wake of tabs. Recently, Sun *et al.* (2012) used 3D tomographic PIV to study vortical structures in the wake of a micro-ramp in a supersonic turbulent boundary layer at Mach number $M = 2$ and $Re_h = 140\,000$. They showed a complex interaction between the CVP and the arc-shaped vortices, where the intermittent arc-shaped vortices result in reducing the distance between the cores of the CVP. Ye, Schrijer & Scarano (2016) studied the transition to turbulence behind a micro-ramp at $Re_h = 1170$; using tomographic PIV, they showed the presence of the primary CVP and arc-shaped vortices. Furthermore, they showed a sidewise development of secondary and tertiary streamwise vortex pairs.

While experimental 3D PIV measurements have revealed the topology of vortical structures in the wake of micro-ramps, similar studies remain needed to unravel the vortical structure organization in the wakes of tabs. Moreover, the vortex dynamics have been mostly studied for trapezoidal tabs, leaving a gap on the effect of tab geometry on the primary and secondary vortices. In this work, we experimentally study the near-wake region behind rectangular, trapezoidal, triangular and ellipsoidal tabs using volumetric PIV at two Reynolds numbers, $Re_h \sim 2000$ and $Re_h \sim 13\,000$. The geometries are chosen such that the trailing tab edge exhibits a reduction in vertex points. We further employ high-spatial-resolution planar PIV to get a closer look at the turbulence statistics and flow instabilities. We aim to highlight and uncover the effect of tab geometry and incoming flow regime (laminar versus turbulent) on the vortical structures and turbulence statistics; we revisit the vortex interaction models discussed earlier and adjust them through experimental evidence. The experimental set-up is described in § 2; the results are analysed and discussed in § 3; and the main conclusions of this work are presented in § 4.

2. Experimental set-up

2.1. *Geometry and flow conditions*

The flow past trapezoidal, rectangular, triangular and ellipsoidal tabs was experimentally studied using volumetric and high-spatial-resolution planar PIV in a 2.5 m long refractive-index-matching (RIM) channel. The flume has a square cross-section of 112.5 mm × 112.5 mm and free-stream turbulence intensity $\sigma_u/U_0 < 0.7\,\%$ for $Re_h = 13\,000$ and $\sigma_u/U_0 \simeq 0$ for $Re_h = 2000$. Here, σ_u and U_0 denote the standard

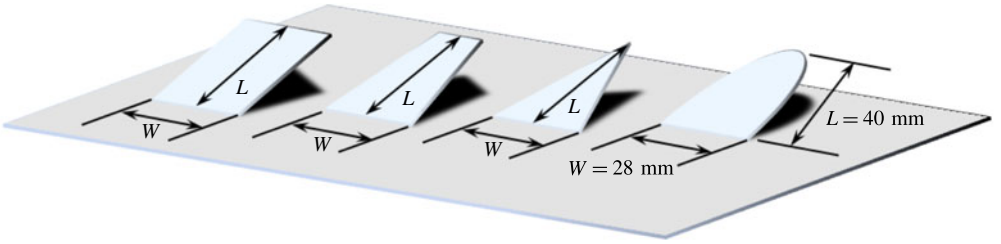

FIGURE 1. (Colour online) Basic dimensions of the rectangular, trapezoidal, triangular and ellipsoidal tabs under study. They share the same base width $W = 28$ mm, length $L = 40$ mm and inclination angle $\alpha = 24.5°$.

deviations of the velocity fluctuations and free-stream velocity. All the tabs were built from smooth acrylic plates with 1.6 mm thickness. They shared the same bulk geometry, i.e. inclination angle $\alpha = 24.5°$, base width $W = 28$ mm, length $L = 40$ mm and height $h = 17$ mm as indicated in figure 1. The inclination angle of the tabs ($\alpha = 24.5°$) and the taper angle of the trapezoidal tab (7.6°) are chosen to match one of the cases studied by Dong & Meng (2004), allowing for insightful comparison. The tabs were attached to the sidewall of the RIM channel (as shown in the schematics) 700 mm ($41h$) from the inlet for the volumetric measurements and 1500 mm ($90h$) for the planar measurements. The volumetric measurements were added to get additional insight on the 3D characteristics of the vortical structures and differences across tab geometries. Therefore, these measurements were made at an upstream location to ensure minimum boundary layer effects. The planar measurements were made at the centreline of the tab (and channel), and therefore the bottom and top wall boundary layers are determined to have a minimal effect on the flow statistics. The tabs were fixed to a flat plate that spanned the channel length and had an elliptical leading edge at the inlet to minimize disturbances to the flow. Through fine temperature control, the refractive index of the working fluid (NaI aqueous solution, $\sim$63 % by weight) was carefully matched to that of the tabs, rendering them nearly invisible. RIM granted full optical access with minimized reflections, allowing for measurements near and under the tabs. The NaI solution has a density of $\rho_0 = 1800$ kg m^{-3} and a kinematic viscosity $\nu \simeq 1.1 \times 10^{-6}$ m^2 s^{-1}. For further details on the channel and the RIM technique, the reader is referred to Blois *et al.* (2012), Bai & Katz (2014) and Hamed *et al.* (2015). Each of the three tabs was studied at two Reynolds numbers, $Re_h = U_0 h/\nu \simeq 2000$ (henceforth low Re) and 13000 (henceforth high Re). Here, U_0 is the incoming free-stream velocity preceding the tab. For both measurement locations, the incoming boundary layer was laminar at the low Re and turbulent at the high Re. As such, the distinctive behaviour observed across Re_h is indicative of the impact of the incoming flow regime. At the location of the planar measurements, the boundary layer had a thickness $\delta_{99}/h = 0.9$ and 1.4 at the low and high Re_h, while $\delta_{99}/h \sim 0.7$ for the volumetric measurements. It is important to note that δ_{99}/h is a key parameter in determining the response of the boundary layer to the tabs. Here, δ_{99}/h is held constant for each case across the four tab geometries, allowing for meaningful comparisons. A summary of the experiments and flow conditions is given in table 1. Figure 2 illustrates the incoming boundary layer profile and turbulence statistics (when appropriate) for both Reynolds numbers at the tab location for the volumetric measurements. Figure 3 shows similar quantities at the location of the planar measurements.

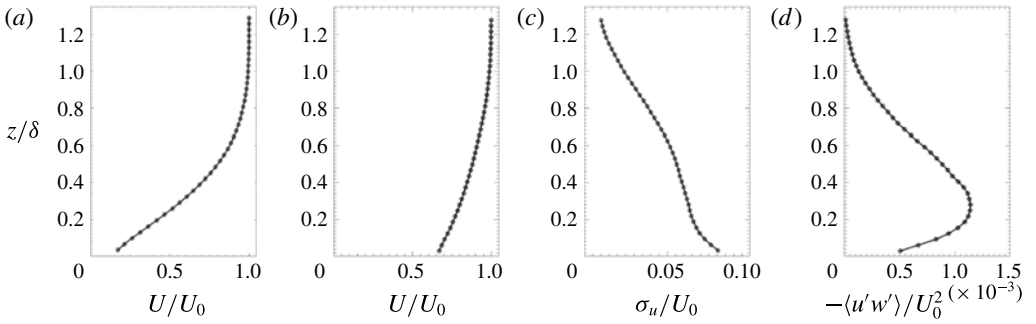

FIGURE 2. Incoming boundary layer statistics at the volumetric measurement location: (*a*) time-averaged streamwise velocity profile U/U_0 for the low Re; (*b*) time-averaged streamwise velocity profile U/U_0 for the high Re; (*c*) turbulence intensity σ_u/U_0 for the high Re; (*d*) Reynolds shear stress $-\langle u'w'\rangle/U_0^2$ for the high Re.

Tab	Measurement	Re_h	U_0 (m s^{-1})	Number of realizations	Vector grid spacing (mm)
Rectangular	Volumetric	1900	0.12	2500	2
		12 200	0.79	2500	2
	Planar	2000	0.13	4000	0.38
		13 100	0.85	4000	0.38
Trapezoidal	Volumetric	2000	0.13	2500	2
		12 400	0.80	2500	2
	Planar	2000	0.13	4000	0.38
		13 000	0.84	4000	0.38
Triangular	Volumetric	2000	0.13	2500	2
		12 500	0.81	2500	2
	Planar	2000	0.13	4000	0.38
		13 000	0.84	4000	0.38
Ellipsoidal	Volumetric	2000	0.13	2500	2
		12 400	0.80	2500	2
	Planar	2000	0.13	4000	0.38
		13 100	0.85	4000	0.38

TABLE 1. Experimental parameters and flow conditions.

2.2. *Volumetric PIV set-up*

The volumetric, three-component velocity measurements were made using a three-camera V3V system from TSI. This measurement technique was developed by Pereira *et al.* (2000) and relies on the use of two or more camera apertures to obtain multiple images of scattering sources. The images are then used to obtain 3D displacements through multiple particle detection and tracking algorithms. In short, a three-step scheme is followed to obtain the volumetric, three-component velocity field from an image pair. First, the two-dimensional (2D) location in each of the six images (three cameras and two consecutive frames) is determined through a particle identification algorithm. In the next step, the 2D locations of the identified particles are used, along with a multi-plane calibration, to locate them in 3D space. Finally,

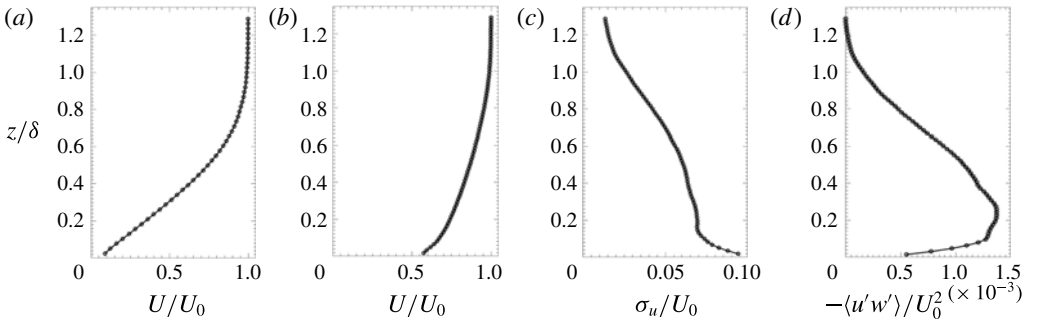

FIGURE 3. Incoming boundary layer statistics at the planar measurement location: (*a*) time-averaged streamwise velocity profile U/U_0 for the low *Re*; (*b*) time-averaged streamwise velocity profile U/U_0 for the high *Re*; (*c*) turbulence intensity σ_u/U_0 for the high *Re*; (*d*) Reynolds shear stress $-\langle u'w'\rangle/U_0^2$ for the high *Re*.

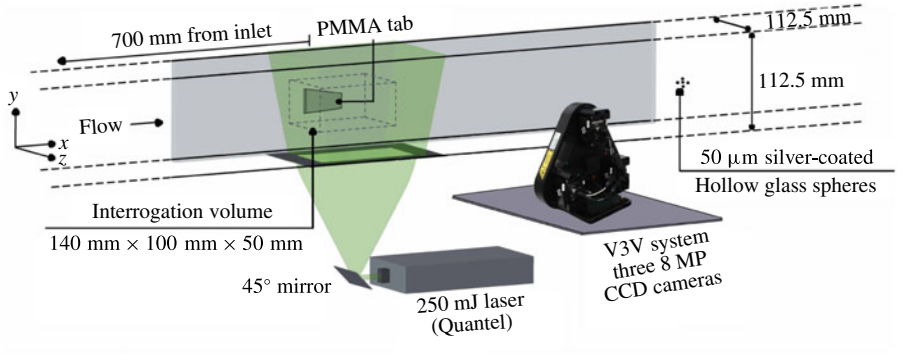

FIGURE 4. (Colour online) Schematics of the experimental set-up for the volumetric PIV measurements.

the velocity is found through particle tracking across the two consecutive frames and then interpolated onto a rectangular grid. The reader is referred to Troolin & Longmire (2009), Sharp *et al.* (2010) and Chamorro *et al.* (2013) for more details on the interrogation scheme. The V3V system has recently been used for volumetric flow measurements in different studies. For example, Chamorro *et al.* (2013) utilized this technique to study the vortical structures in the wake of a hydrokinetic turbine. Other examples include the study of vorticity dynamics in revolving wings (Cheng *et al.* 2013), jet flows (Cambonie, Gautier & Aider 2013) and vortical structures generated by plunging wings (Calderon *et al.* 2013). The system employed in this study consisted of three 8 MP (3320 × 2496 pixels), 12-bit, frame-straddle, charge-coupled device (CCD) cameras fixed within a frame as shown in figure 4. The flow was seeded with 50 μm silver-coated hollow glass spheres. The measurement volume was set to 140 mm × 100 mm × 50 mm ($x \times y \times z$) and was illuminated using a laser volume supplied by a 250 mJ pulse^{-1} double-pulsed Quantel laser. For each of the eight cases (four tabs, two *Re*), 2500 image pairs were captured at a frequency of 2 Hz and later processed using the Insight V3V software from TSI following the aforementioned scheme. The interrogation voxel had a size of 8 mm × 8 mm × 8 mm with 70 % overlap, resulting in a final vector grid spacing $\Delta x = \Delta y = \Delta z \simeq 2$ mm after

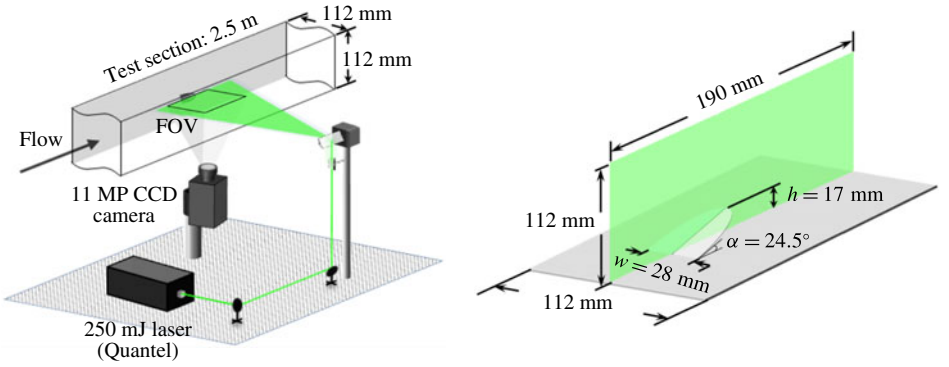

FIGURE 5. (Colour online) Schematics of the experimental set-up and details of the field of view for the planar PIV measurements.

interpolation onto a rectangular grid. A typical image pair resulted in approximately 22 000 independent randomly spaced velocity vectors. Pereira & Gharib (2002) estimated the uncertainty to be less than 1 % in the streamwise and spanwise velocity components and less than 4 % in the wall-normal component for a set-up similar to the one shown in figure 4. This implies an uncertainty less than 6 % in the vortex circulation discussed below. These measurements were used to investigate the large-scale vortices formed downstream of the tabs, and therefore the 50 μm particles are determined to be sufficient for this purpose. The spatial resolution of the volumetric measurements results in coarser estimation of the velocity gradients compared to those of the planar counterpart. However, the resolution is sufficient to provide meaningful comparison across the various tabs.

2.3. *Planar high-spatial-resolution PIV set-up*

The high-resolution 2D PIV measurements were made in a streamwise wall-normal plane (x–z) coinciding with the centre of both the tab and the channel. Measurements were obtained with a planar system from TSI. The working fluid was seeded with 14 μm silver-coated hollow glass spheres. A field of view (FOV) 190 mm × 112 mm was illuminated using a 1 mm thick laser sheet supplied by a 250 mJ pulse^{-1} double-pulsed laser from Quantel. Four thousand image pairs for each case (four tabs, two Re_h) were captured at a frequency of 1 Hz by an 11 MP, 12-bit, frame-straddle, CCD camera. Figure 5 shows the schematics of the experimental set-up, including the FOV details. Image pairs were interrogated with a recursive cross-correlation method using the Insight 4G software package from TSI. The final interrogation window was 16 × 16 pixels with 50 % overlap, resulting in a final vector grid spacing $\Delta x = \Delta z = 380$ μm. These measurements were used to acquire detailed, well-resolved turbulence statistics and to capture instability mechanisms in the shear layer downstream of the tabs.

3. Results and discussion

In this section we present the common and distinctive flow statistics and dominant vortical structures for the rectangular, trapezoidal, triangular and ellipsoidal tabs at the low and high Re_h. Owing to the extensive experimental effort (four tab

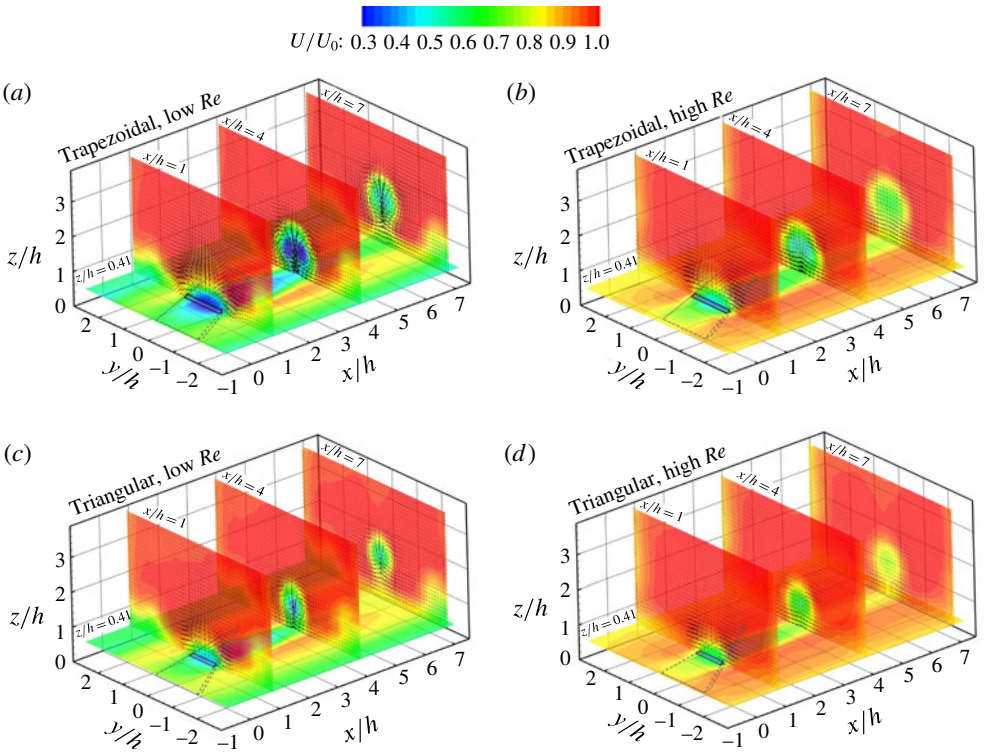

FIGURE 6. (Colour online) Time-averaged streamwise velocity U/U_0 contours in vertical y–z planes at $x/h = 1$, 4 and 7 and in the wall-parallel x–y plane at $z/h = 0.41$ obtained from volumetric PIV measurements. Vectors indicate in-plane velocity field. (*a*,*b*) Trapezoidal tab, low and high Re_h, respectively. (*c*,*d*) Triangular tab, low and high Re_h, respectively.

geometries, two Reynolds numbers and two measurement techniques) and for brevity, we highlight only selected representative cases without compromising the overall discussion. Although the tabs share various geometrical features, including base width, height and inclination angle, their different frontal geometries lead to distinctive characteristics and streamwise evolution of the vortical structures in the wake. First, the impact of the geometry and Reynolds number on the mean flow past the tabs is illustrated in figures 6–10. The normalized time-averaged streamwise velocity contours U/U_0 for the trapezoidal and triangular tabs are shown in figure 6 within the vertical y–z planes at $x/h = 1$, 4 and 7 and in the wall-parallel x–y plane at $z/h = 0.41$. In figure 6 and subsequent ones, the centre of the tab base is located at (0, 0, 0), the velocity vectors indicate in-plane flow field and the wall-parallel plane at $z/h = 0.41$ marks the lower boundary of the volumetric measurement region. For the two tabs shown in figure 6, and the other two which are not shown for brevity, the velocity distribution is dependent on the incoming flow regime (laminar versus turbulent), where the normalized deficit is reduced for each tab at the higher Re_h (turbulent incoming flow). Furthermore, the larger frontal area of the trapezoidal tab (figure 6*a*,*b*) compared to the triangular one (figure 6*c*,*d*) leads, as expected, to a larger normalized flow deficit and near-wake size across both Reynolds numbers. This dependence on the flow-facing tab area was observed for the other tabs as well.

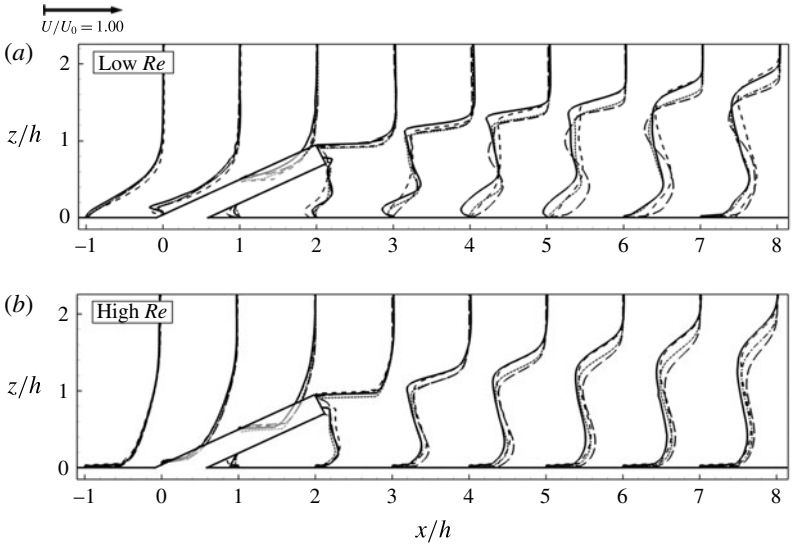

FIGURE 7. Time-averaged streamwise velocity U/U_0 profiles at the central plane of the four tabs at the low and high Re_h. The results are obtained from high-spatial-resolution planar PIV. The velocity profiles are taken at the locations indicated in the abscissa and lines indicate rectangular (continuous), trapezoidal (dashed), triangular (dot-dashed) and ellipsoidal (long-dashed) tabs.

The flow-facing tab areas as a percentage of that of the rectangular tab are 81 %, 79 % and 50 % for the trapezoidal, ellipsoidal and triangular tabs, respectively.

The U/U_0 profiles, shown in figure 7 and obtained using high-spatial-resolution planar PIV at the central plane of the four tabs, highlight the higher sensitivity of the flow field to the tab geometry at the low Re_h. Only the rectangular tab exhibits flow reversal near the wall for $\sim 3h$ downstream of the tab edge. The inflection points of the velocity profile differ in their vertical location across the tab geometry at the low Re_h. Yang *et al.* (2001) showed for a trapezoidal tab that the inflection point near $z/h = 1$ is associated with the hairpin vortex head while the lower inflection point is associated with a secondary vortical structure with an opposite sense of rotation to the hairpin vortex head. Furthermore, the mean shear, $\partial U/\partial z$, at the tab height is significantly enhanced at the low Re_h, promoting KH instability, whose effects will be shown below. At the base of the tabs (figure 7), upstream flow reversal is observed at the low Re_h, giving rise to the 'necklace' vortex that was first observed in the simulations of Dong & Meng (2004). However, this recirculation region is not present at the high Re_h.

The normalized time-averaged spanwise V/U_0 and wall-normal W/U_0 velocity distributions for the trapezoidal tab at both Re_h, shown in figures 8 and 9, reveal the signature of the CVP that induces significant mean spanwise flow, and upward wall-normal entrainment at the tab symmetry plane. The spanwise flow V reaches up to $\sim 0.17U_0$ at the low Re_h and exhibits a decrease in the overall distribution at the high Re_h (figure 8). An upward flow is formed in the region between the two branches of the CVP and reaches up to $\sim 0.15U_0$ at the symmetry plane at the low Re_h (figure 9). This upward flow is essential in the mixing and transport of near-wall fluid into the free-stream flow (Dong & Meng 2004). Similar to the spanwise component, W/U_0 is significantly lower at the high Re_h. The reduction in V/U_0 and W/U_0 at the high Re_h was also observed for the other tabs. To further

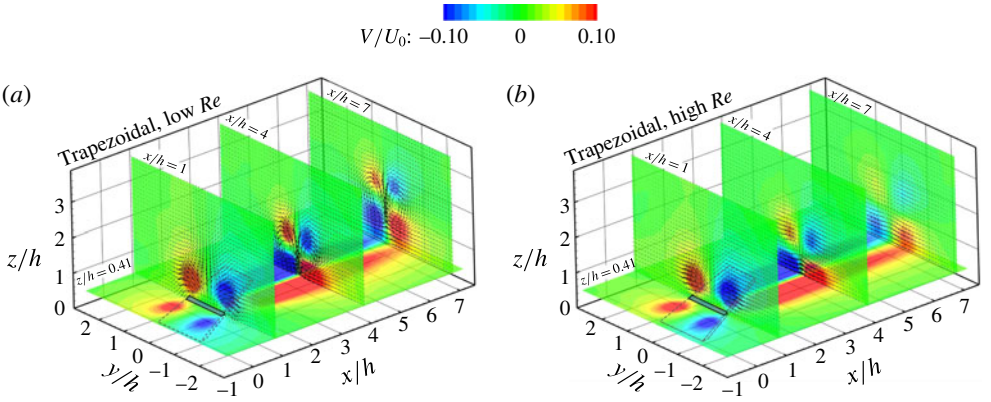

FIGURE 8. (Colour online) Time-averaged spanwise velocity V/U_0 contours for the trapezoidal tab at the low (*a*) and high (*b*) Re_h in vertical *y*–*z* planes at $x/h = 1$, 4 and 7 and in the wall-parallel *x*–*y* plane at $z/h = 0.41$ obtained from volumetric PIV measurements. Vectors indicate in-plane velocity field.

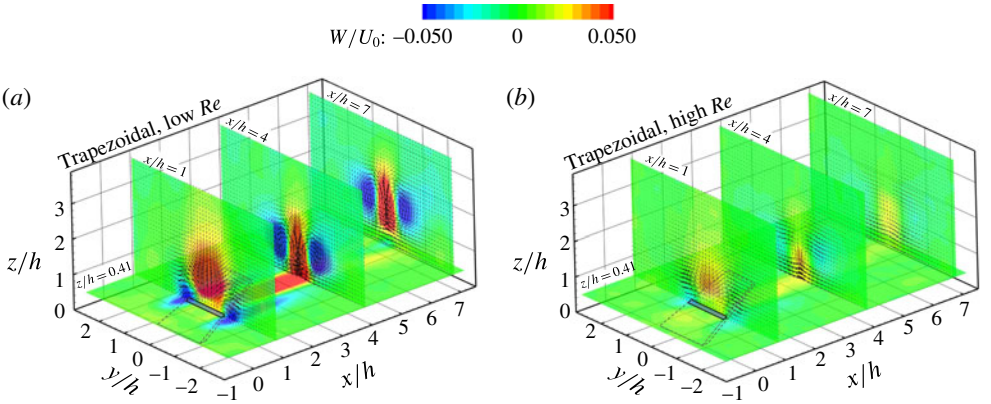

FIGURE 9. (Colour online) Time-averaged wall-normal velocity W/U_0 contours for the trapezoidal tab at the low (*a*) and high (*b*) Re_h in vertical *y*–*z* planes at $x/h = 1$, 4 and 7 and in the wall-parallel *x*–*y* plane at $z/h = 0.41$ obtained from volumetric PIV measurements. Vectors indicate in-plane velocity field.

inspect the effect of Reynolds number and tab geometry on the vertical flow, figure 10 shows one-dimensional (1D) profiles of W/U_0 at $z/h = 1$ (tab tip) for the four tabs at both Re_h. Despite some spanwise asymmetry, probably a result of multiple factors, fair comparison across the different tab geometries is provided from these profiles. Upstream of $x/h = 2$, the region of enhanced vertical flow is mainly due to the inclined geometry of the tabs. Beyond $x/h = 2$, the enhanced vertical flow is due to the common-up entrainment induced by the CVP and the upward pumping by intermittent hairpin vortices. These two primary vortical structures are discussed in detail below. Overall, the vertical flow is reduced at the high Re_h, with the triangular tab showing the lowest wall-normal flow across both Re_h. At the low Re_h, the rectangular and trapezoidal tabs maintain higher wall-normal flow; while at the high Re_h, the rectangular tab performs better than the other tabs.

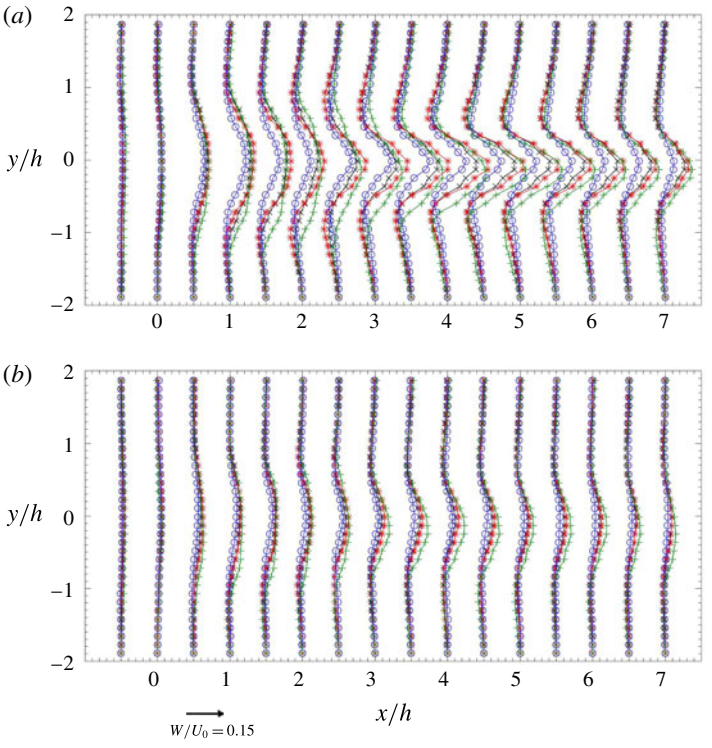

FIGURE 10. (Colour online) Time-averaged wall-normal velocity W/U_0 profiles at $z/h = 1$ (i.e. tab tip) for the four tabs at the low (*a*) and high (*b*) Re_h. The results are obtained from the volumetric PIV measurements. Colours indicate profiles from the rectangular (green +), trapezoidal (red ∗), triangular (blue ◯) and ellipsoidal (black ×) tabs.

The 3D topology of the CVP, which forms due to the pressure drop across the tabs (Dong & Meng 2004), is illustrated for the trapezoidal tab at both Re_h in figure 11 through isosurfaces of the normalized x-vorticity $\omega_x h/U_0 = \pm 0.1$ with superimposed V/U_0 planar contours. In contrast to the hairpin vortices, the CVP is present in the mean flow field and, as such, ω_x is here calculated using the time-averaged flow field (V, W). The structures in figure 11 were also visualized using the Q (Hunt, Wray & Moin 1988) and λ_2 (Jeong & Hussain 1995) criteria and showed similar topology. It is noted that, at the low Re_h, a secondary CVP with an opposite sense of pair rotation to that of the primary one is observed downstream of $x/h = 5$ (figure 11*a*). This secondary structure was observed in the simulations of Dong & Meng (2004) and Habchi *et al.* (2010*b*) and was identified as detrimental to mixing, as it induces a downward flow in the symmetry axis of the tab. We provide experimental evidence of this secondary structure appearing at the low Re_h; however, this structure was not observed at the high Re_h. In fact, this structure was observed for all tabs at the low Re_h but for none at the high Re_h. It is likely that the more prominent wall vortical structures at the high Re result in reducing the coherence of this near-wall secondary CVP. Additional measurements of higher resolution are needed to investigate the presence of this structure. As seen in figure 11, the primary CVP is inclined at a higher angle at the low Re_h, possibly due to the presence of the secondary CVP and the lower advection at the low Re_h. Following a procedure similar to that of

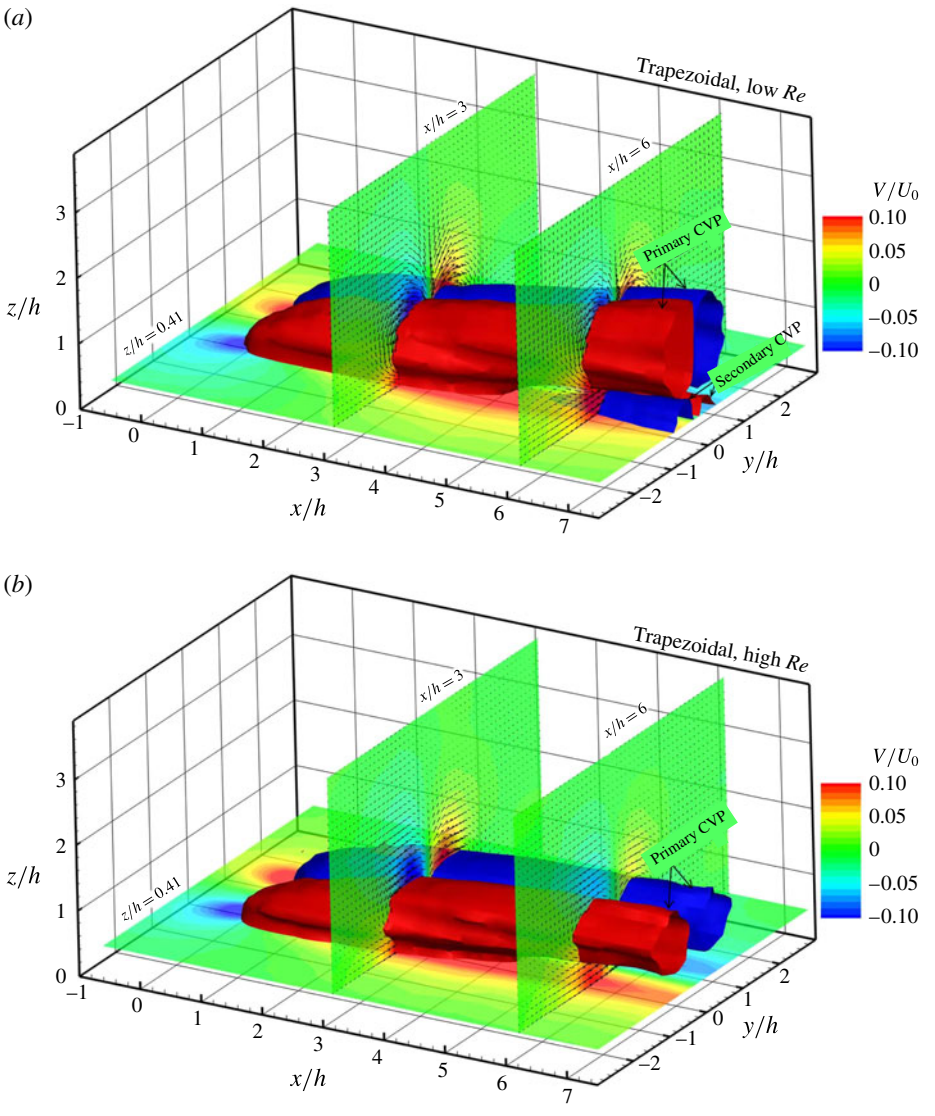

FIGURE 11. (Colour online) The counter-rotating vortex pair in the wake of the trapezoidal tab illustrated with x-vorticity isosurfaces $\omega_x h/U_0 = +0.1$ (red) and -0.1 (blue) at the low (a) and high (b) Re_h. The V/U_0 contours and in-plane velocity vector fields in y–z planes at $x/h = 3$ and 6 and in the x–y plane at $z/h = 0.41$ are superimposed for clarity. The results are obtained from the volumetric PIV measurements.

Lögdberg, Fransson & Alfredsson (2009) and Habchi *et al.* (2010*b*), the location of the core of the CVP is identified as the point of maximum Q_x, where

$$Q_x = -\frac{1}{2}\frac{\partial W}{\partial y}\frac{\partial V}{\partial z} \tag{3.1}$$

is the second invariant of the 2D velocity gradient tensor calculated locally in a given y–z plane. In figure 12, the height of the core for both branches is averaged and shows steeper slope at the low Reynolds number across all tabs.

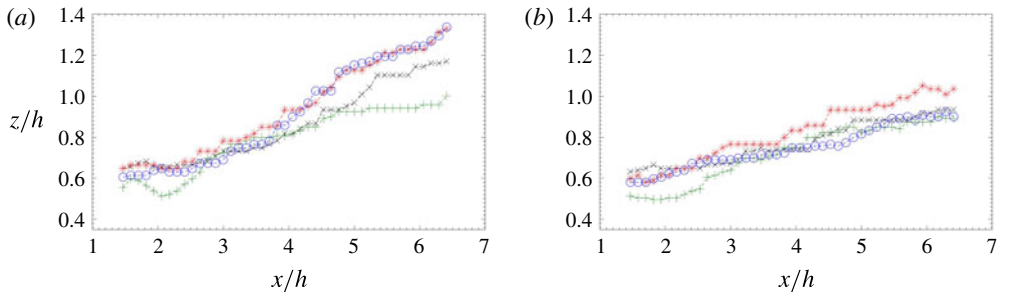

FIGURE 12. (Colour online) Streamwise evolution of the vertical location z/h of the CVP core averaged across both branches at the low (*a*) and high (*b*) Re_h. Results are from the volumetric PIV measurements for the rectangular (green +), trapezoidal (red ∗), triangular (blue ◯) and ellipsoidal (black ×) tabs.

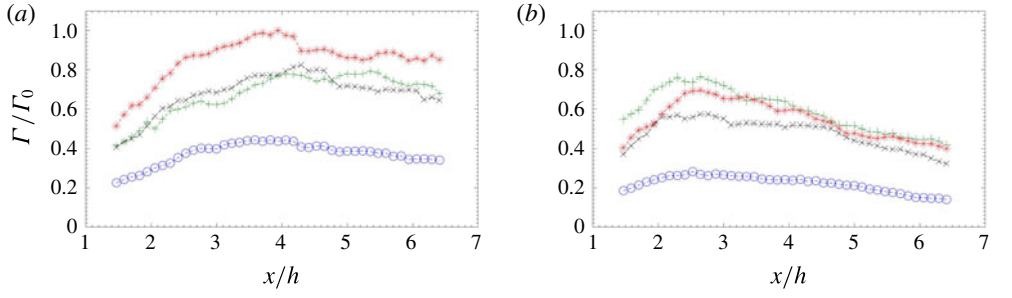

FIGURE 13. (Colour online) Streamwise evolution of the normalized circulation Γ/Γ_0 averaged across both branches of the CVP at the low (*a*) and high (*b*) Re_h. Results are from the volumetric PIV measurements for the rectangular (green +), trapezoidal (red ∗), triangular (blue ◯) and ellipsoidal (black ×) tabs.

Further, the circulation

$$\Gamma = \int_A |\omega_x| \frac{h}{U_0} \, \mathrm{d}A \tag{3.2}$$

is calculated locally at each y–z plane. Here, $|\omega_x|h/U_0$ is the normalized vorticity in the x-direction and A is the normalized area of the vortex defined as the region where Q_x drops to 5 % of its maximum value at the core (Lögdberg *et al.* 2009; Habchi *et al.* 2010*b*). Figure 13 shows the circulation for all tabs at the two Re_h averaged across both branches and normalized by the global maximum, Γ_0, which occurs for the trapezoidal tab at $x/h \sim 4$ at the low Re_h. Larger circulation and slower decay are observed at the low Re_h. This is attributed to the reduced background turbulence from the incoming boundary layer flow (shown in figure 17), which reduces the coherence of the vortical structures induced by the tabs. Consequently, the reduced coherence and circulation at the high Re_h lead to the lower mean spanwise and wall-normal flows discussed earlier. The strength of the CVP exhibits distinctive streamwise evolution across Reynolds number. At the low Re_h, continuous growth in Γ/Γ_0 is observed until a maximum occurs at $x/h \sim 4$, while the maximum is reached significantly earlier at $x/h \sim 2.5$ at the high Re_h. The lower incoming flow turbulence at the low Re_h allows for the coherence and strength of the CVP to be preserved for a larger downstream distance. Owing to the important role of the CVP in mixing, the

distinctive behaviour and topology across Re_h suggests higher efficiency through CVP mixing at the low Re_h. Moreover, when such tabs are placed in rows, the spacing must be chosen carefully in correspondence with the operating Re_h to maintain energetic steady mixing. Given that the CVP originates due to the pressure drop, it is expected that tab blockage affects the strength of the CVP. However, as seen in figure 13, the normalized circulation does not directly correspond to blockage and is shown to be highly dependent on geometry and incoming flow regime. This suggests the need for application-specific testing when choosing a tab geometry where mixing by the CVP is desired.

Quasi-periodic hairpin vortices in the wake of trapezoidal tabs have been reported through 2D flow visualizations and planar PIV (Elavarasan & Meng 2000; Yang *et al.* 2001). However, the 2D character of these measurements falls short in its ability to describe the 3D topology of the hairpin vortices and their interaction with the CVP. Although limited to a low $Re_h = 600$, the DNS simulations by Dong & Meng (2004) have greatly advanced the understanding of these structures. They observed that the hairpin vortex heads are rolled from the shear layer formed at the trailing edge of the tab. Moreover, they suggested splitting and deformation as the mechanism responsible for transforming the CVP into the hairpin vortex legs. Our volumetric PIV measurements show the hairpin vortices and their interaction with the CVP at a Re_h one order of magnitude higher than that of Dong & Meng (2004). Furthermore, our measurements show that the CVP does not necessarily evolve into the hairpin legs, and that there are various forms of interaction. Figure 14 illustrates a representative instant where the coexistence of the hairpin structures and the CVP takes place in the wake of the ellipsoidal tab at $Re_h = 2000$. There, the hairpin structures are identified using an isosurface of the normalized vorticity magnitude $|\omega|h/U_0 = 1.2$. Two stream traces (with $u - u_c$, v, w, where u_c is the velocity at the core of the downstream hairpin head) are shown to highlight the flow direction and circulation at the hairpin head. The instantaneous CVP (in contrast to the mean one in figure 11) is identified using an isosurface of the normalized Q criterion $Q_x h^2/U_0^2 = 0.02$, where Q_x is calculated at consecutive y–z planes using (3.1). Note that, for figure 14, both ω and Q_x are calculated based on the instantaneous flow field (u, v, w). While hairpin vortices were observed for all tabs, we illustrate here those in the wake of an ellipsoidal tab to show that a flat trailing edge is not a necessary condition for the generation of hairpin vortices. This is in contrast with the work of Gretta (1990), who suggested the need for a flat tab trailing edge for the generation of hairpin vortices. However, we point out that a flat edge is likely to enhance the shear, $\partial u/\partial z$, leading to stronger hairpin vortices, as discussed in the context of the 2D measurements below. As seen in figure 14, hairpin vortices coexist and interact with the CVP. Although the CVP is influenced and deformed due to this interaction, it remains present, in contrast with the observations of Dong & Meng (2004). An enlarged view of the region $6 \leqslant x/h \leqslant 7$ is given in figure 15 and suggests at least two forms of interaction between the hairpin vortex legs and CVP structures. The region A (figure 15*a*) highlights the coexistence, and not merging, of the hairpin leg with the CVP. The branch of the CVP with negative streamwise vorticity continues past the hairpin head, while the branch with positive streamwise vorticity undergoes deformation and splits around the hairpin head, as seen in region B (figure 15*b*). Similar instantaneous interactions have been observed for the other tabs. High-frame-rate measurements are needed to further investigate the temporal behaviour of these large-scale vortices. Such measurements would allow for a better description of the interaction of the CVP with the hairpin vortices.

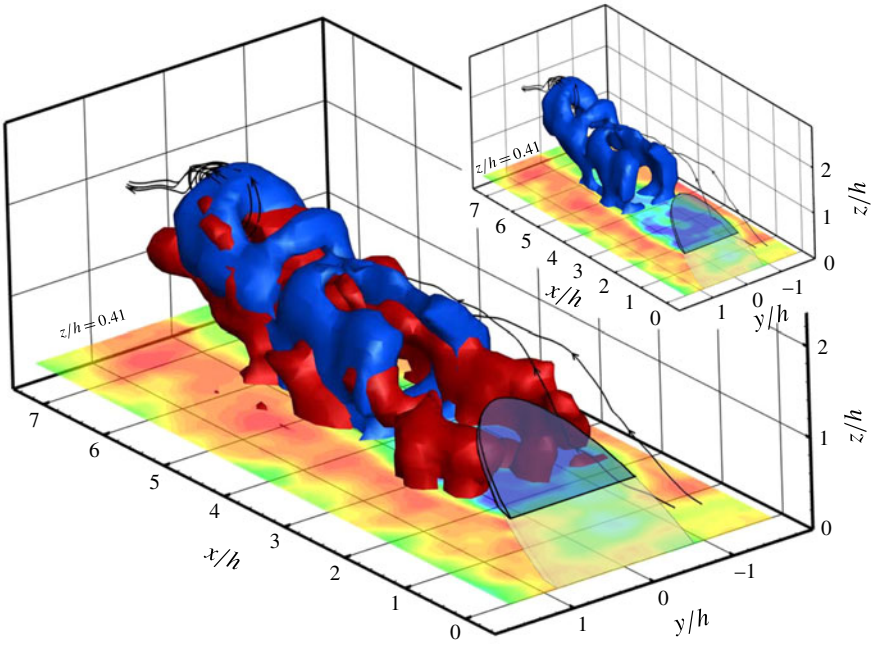

FIGURE 14. (Colour online) Coexistence of hairpin vortices with CVP in the wake of an ellipsoidal tab at the low Re_h. Hairpin structures (in blue) are identified using the $|\omega|h/U_0 = 1.2$ isosurface. CVP (in red) is identified using the $Q_x h^2/U_0^2 = 0.02$ isosurface. Two stream traces (with $u - u_c$, v, w, where u_c is the velocity at the core of the hairpin head) are shown to depict the sense of rotation. The levels for the u/U_0 contours in the wall-parallel x–y plane at $z/h = 0.41$ are the same as in figure 6. The results are obtained from volumetric PIV measurements; the hairpin vortices without the CVP are shown in the top right corner for clarity.

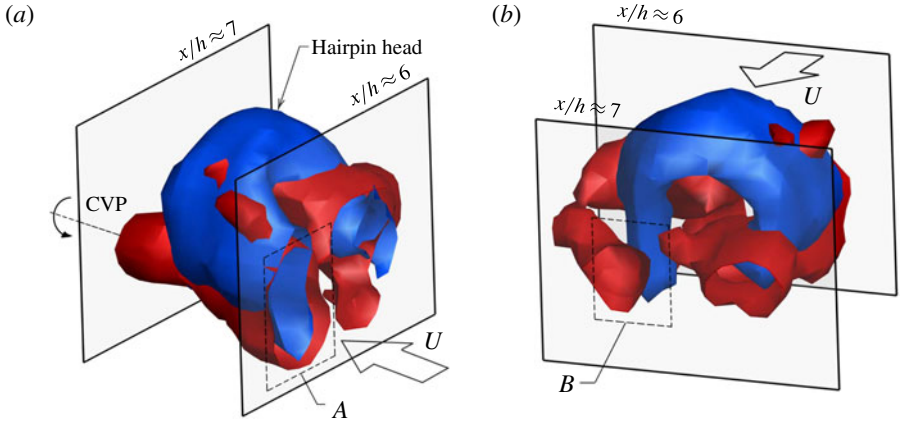

FIGURE 15. (Colour online) Enlarged view from figure 14 around $6 \lesssim x/h \lesssim 7$ illustrating the interaction between the hairpin vortex and CVP.

Further insight into the formation, dynamics and trajectory of the heads of the hairpin vortices is gained from the representative instantaneous signed swirling

	Rectangular	Trapezoidal	Triangular	Ellipsoidal
$\bar{\Gamma}/(U_0h)$	0.39	0.21	0.22	0.29
$[\bar{\Gamma}/(U_0h)]/[\bar{\Gamma}/(U_0h)]_r$	1	0.53	0.57	0.74
$\bar{r}_c/h$	0.12	0.10	0.11	0.11
$\bar{r}_c/r_{c,r}$	1	0.83	0.92	0.92

TABLE 2. Normalized average circulation $\bar{\Gamma}/(U_0h)$ and vortex core radius $\bar{r}_c/h$ of hairpin heads observed within $5.5 \leqslant x/h \leqslant 7.5$ for the four tabs at the low Re_h. Subindex r indicates a quantity from the rectangular tab.

strength $\Lambda_{ci}h/U_0$ fields obtained from the 2D high-resolution measurements given in figure 16. Here Λ_{ci} is the magnitude of the imaginary part of the complex eigenvalues of the velocity gradient tensor (Zhou *et al.* 1999) and its sign indicates the orientation of the swirl (Wu & Christensen 2006). Figure 16 highlights the generation of hairpin vortices (heads) in the case of triangular and ellipsoidal tabs regardless of their lack of a flat trailing edge. Moreover, figure 16 contrasts the dynamics across Re_h for the four tabs. In particular, the necklace vortex at the upstream edge of the four tabs, illustrated at the top left corner of the rectangular tab at low Re_h, is not present at the high Re_h. At the low Re_h, the high shear, $\partial u/\partial z$, promotes KH instability that manifests in the periodic shedding of hairpin vortices. In fact, the flow is mostly laminar upstream of this location at this Re_h. Interestingly, the geometry affects the location of the onset of hairpin vortices at the low Re_h. A careful review of numerous instantaneous fields suggests that the largest delay in hairpin vortex location occurs for triangular tabs. The vortex dynamics at the high Re_h are remarkably richer due to the turbulent nature of the incoming and wake flows. The entire wake exhibits a high population of vortical structures and lacks the well-formed KH instability observed at the low Re_h. The multi-scale finer structures around the large-scale hairpin vortices affect their strength, path and coherence.

The comparatively low turbulence levels at the low Re_h allow for further comparisons in the strength and scale of the hairpin heads across tab geometries. Following Moriconi (2009), we chose the Lamb–Oseen vortex as a simplified model to represent the head of hairpin vortices identified at the low Re_h in figure 16. The Lamb–Oseen vortex is a non-stationary solution of the Navier–Stokes equations given in cylindrical coordinates as

$$u_\theta(r) = \frac{\Gamma}{2\pi r}[1 - \mathrm{e}^{-r^2/r_c^2}]. \tag{3.3}$$

Here, r_c is the vortex core radius at a given instant and r is the radial distance from the vortex core. Although a simplified model, it shows remarkable agreement with the measured data. To allow for comparisons across different tabs, we compute the normalized mean circulation $\bar{\Gamma}/(U_0h)$ and vortex core radius $\bar{r}_c/h$ for hairpin heads within $5.5 \leqslant x/h \leqslant 7.5$ across 30 instantaneous fields. Both Γ and r_c were obtained from curve fitting individual hairpin heads to the Lamb–Oseen model; $\bar{\Gamma}/(U_0h)$ and $\bar{r}_c/h$ are reported in table 2. The rectangular tab has the highest circulation and core radius, while the triangular tab shows the weaker and smaller hairpin heads. To facilitate comparison, the quantities for the other tabs are scaled by that of the rectangular. There, it is noted that the circulation of the hairpin heads for the

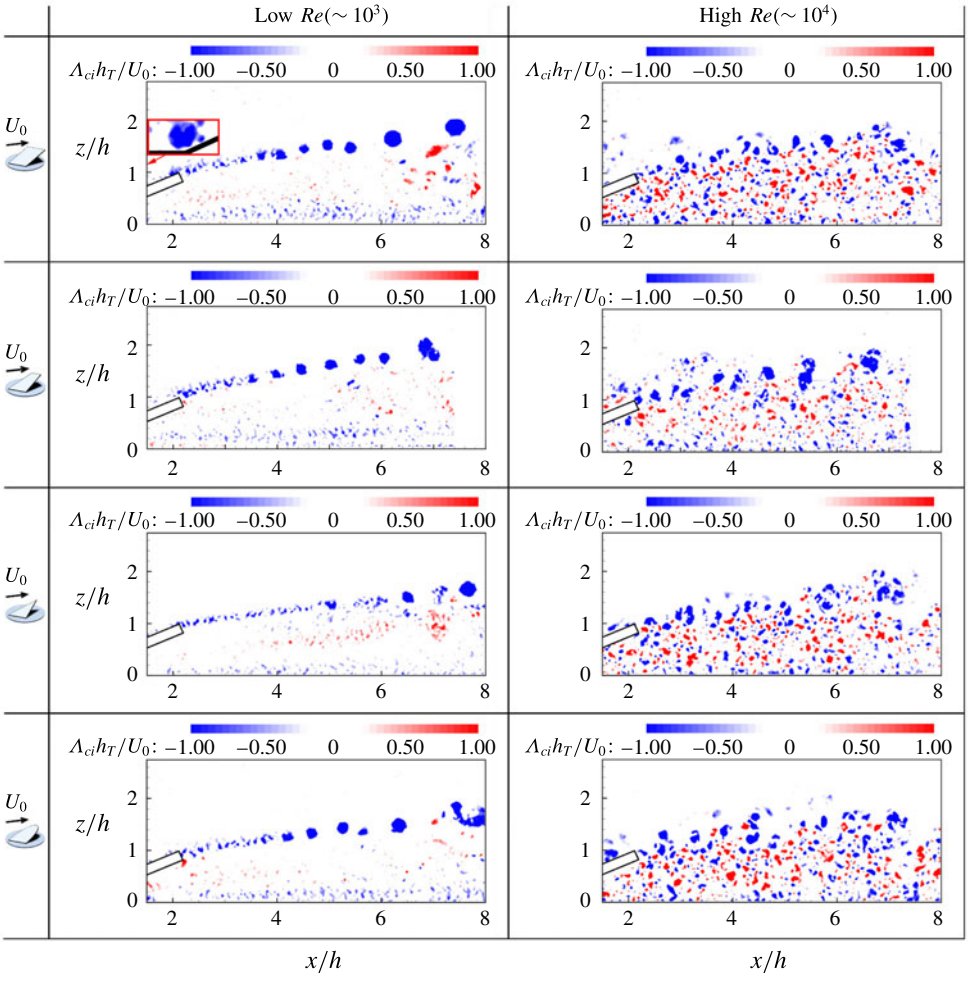

FIGURE 16. (Colour online) Instantaneous signed swirling strength $\Lambda_{ci}h/U_0$ at the central plane of the four tabs at both Re_h. The top left panel shows an example of the necklace vortex formed at the leading edge of the tabs for the low Re cases. The results are obtained from high-spatial-resolution planar PIV measurements.

triangular tab are $\sim 50\,\%$ of those of the rectangular one, but their size is similar (r_c for the triangular tab is 92 % of the rectangular). As reported in table 2, tab geometry, through blockage and trailing edge, plays a significant role in determining the scale and strength of the generated hairpin vortices.

Finally, the turbulent kinetic energy $\mathrm{TKE} = \langle u'^2 + w'^2\rangle/2U_0^2$ and primary Reynolds shear stress $-\langle u'w'\rangle/U_0^2$ obtained from the planar PIV measurements are given in figures 17 and 18 for the four tabs at both Re_h. The figures illustrate the distinctive behaviour of the velocity fluctuations across Re_h. In contrast to the high Re_h case, enhanced turbulence levels are delayed by $\sim(2\text{–}3)h$ behind the downstream edge of the tab. In this region, the high shear promotes KH instability. The reduced turbulence levels within this region along with the delayed generation of hairpin vortices (figure 16) allow the CVP to maintain coherence and growth in strength

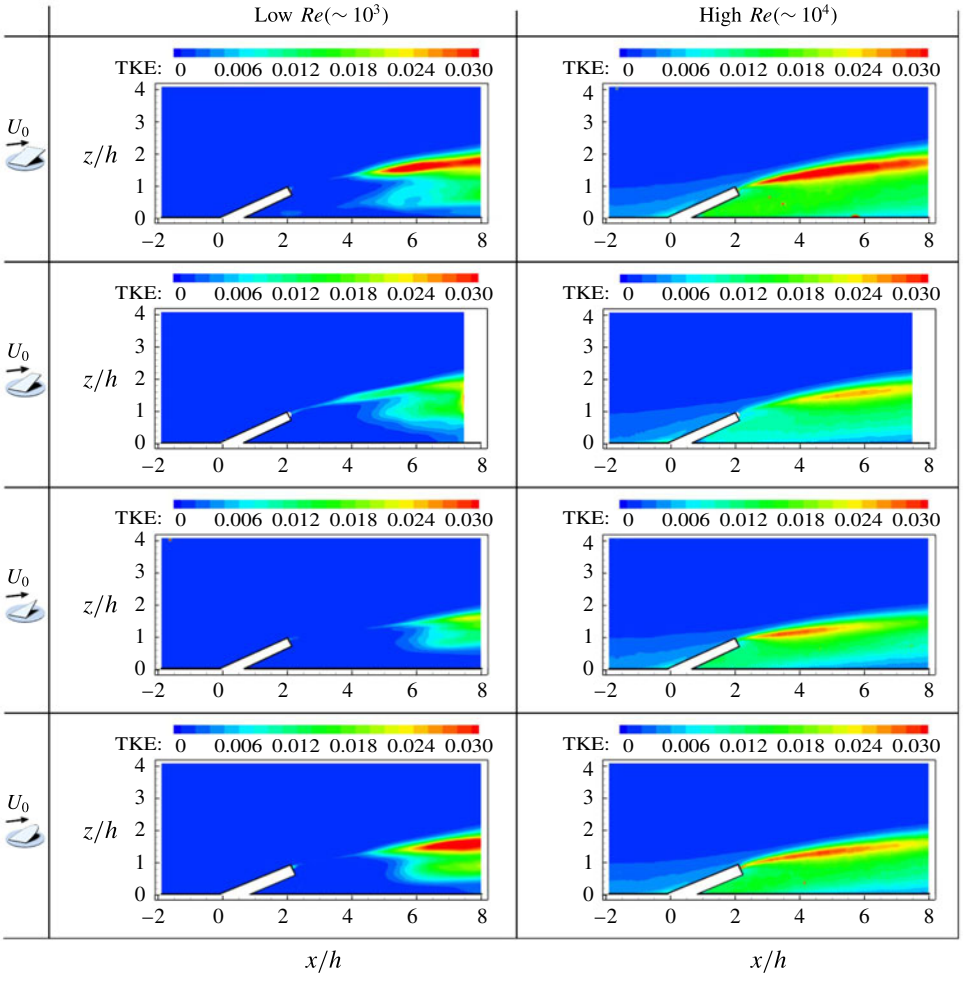

FIGURE 17. (Colour online) Turbulent kinetic energy $\mathrm{TKE} = \langle u'^2 + w'^2 \rangle / 2U_0^2$ fields for the four tabs at both Re_h. The results are obtained from the high-spatial-resolution planar PIV measurements.

in contrast to the high Re_h case (figure 13). Figures 17 and 18 suggest that this instability develops over a larger distance for the triangular tab, which is in line with the mean shear, $\partial U/\partial z$, inferred from figure 7. Dong & Meng (2004) and Habchi *et al.* (2010*b*) have discussed in detail the role of the various vortical structures in mixing. Given the distinctive vortex dynamics across Re_h and tab geometry, the problem of mixing maximization proves to be a complex one best determined at the operational Re_h.

4. Conclusions

We provide 3D PIV measurements of the CVP, hairpin vortices and secondary CVP in the wake of tabs with various geometries. We further offer new evidence on the interaction of these primary and secondary structures. Across the four studied tab

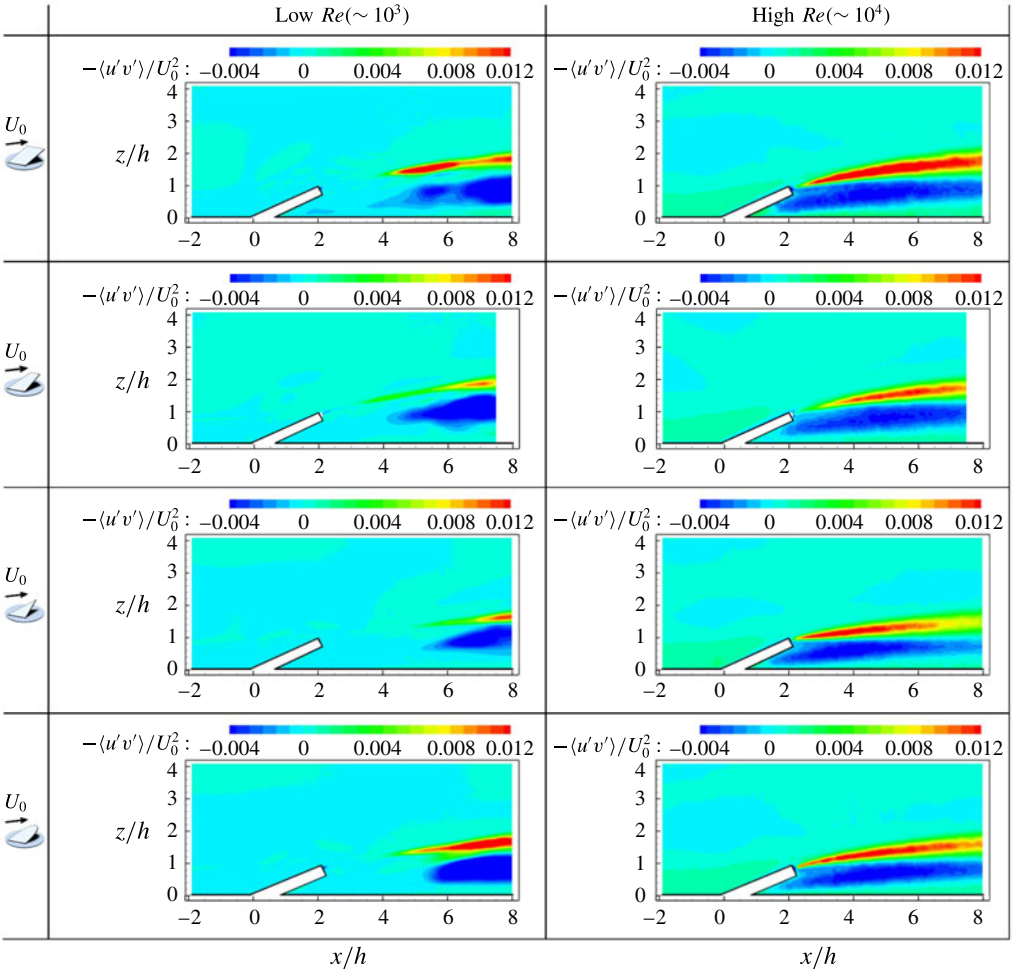

FIGURE 18. (Colour online) Primary Reynolds shear stress $-\langle u'w'\rangle/U_0^2$ fields for the four tabs at both Re_h. The results are obtained from the high-spatial-resolution planar PIV measurements.

geometries and two Re_h, the CVP is coherently present in the mean flow field and leads to significant mean spanwise and wall-normal flows. The topology and strength of the CVP exhibit distinctive behaviour across Reynolds number, where growth in strength is observed for a significantly longer distance and a steeper inclination angle is maintained at the low Re_h across the four tabs. Moreover, a secondary CVP with opposite sense of rotation to that of the primary one is observed for the four tabs only at the low Re_h and is determined to be detrimental to mixing due to its downward flow entrainment at its central plane. The larger circulation of the CVP at the low Re_h is attributed to lower turbulence levels of the incoming flow, which reduce the coherence of the CVP. This larger circulation and enhanced coherence result in comparatively larger mean spanwise and wall-normal flows for the four tabs at the low Re_h. The flow field is shown to be sensitive to the tab geometry. The CVP retains the highest circulation for the trapezoidal tab at the low Re_h, suggesting its superiority in steady mixing through the induced mean spanwise and wall-normal flows. At the low Re_h, the

circulation for the trapezoidal tab is higher than that of the rectangular tab even though it has a significantly lower flow-facing area (81 % of that of the rectangular tab). At the high Re_h, the trapezoidal and rectangular tabs exhibit approximately similar circulation. The triangular tab exhibits the lowest circulation across both Re_h.

In contrast to the work of Gretta (1990), the 2D and 3D measurements presented here provide evidence that hairpin vortices are formed in ellipsoidal and trapezoidal tabs regardless of their lack of a flat trailing edge. However, the presence of a flat trailing edge leads to larger mean shear, $\partial U/\partial z$, and consequently stronger hairpin vortices. The interaction of the CVP with the hairpin vortices for the four tabs at the low Re_h, captured in 3D, shows a complex coexistence of both structures, with the CVP undergoing deformation and splitting at times. In contrast to previous studies, we observe the CVP to remain coherently present regardless of this complex interaction. The high-spatial-resolution PIV measurements at the central plane allowed for the quantification of the strength and scale of the heads of the generated hairpin vortices across the various tabs. The heads at the central plane are found to be in good agreement with the Lamb–Oseen vortex model. Using this formulation, we provide evidence for the ability of rectangular tabs to generate stronger hairpin vortices relative to trapezoidal, triangular and ellipsoidal ones. The generation of hairpin vortices is delayed $\sim(2\text{–}3)h$ at the low Re_h due to the presence of KH instability. Negligible turbulence levels within the instability region allow for the CVP to maintain coherence and growth in strength. While the trapezoidal tab exhibited the highest circulation for the CVP, the hairpin heads in its wake are found to be much weaker than those of the rectangular tab ($\sim$50 % of the rectangular). This evidence suggests the need for heat transfer measurements to indicate which tab is the superior passive mixer in HEV applications. Finally, the considerably distinctive vortex dynamics across Re_h suggests that tab geometry and spacing must be chosen specifically according to the operational incoming flow regime.

Acknowledgements

This work was supported by the Department of Mechanical Science and Engineering, University of Illinois at Urbana-Champaign, as part of the start-up package of Leonardo P. Chamorro. The experiments were performed in a facility built under the National Science Foundation grant award CBET-0923106. The authors are grateful for the help of Dr C. Marsh at the US Army Construction Engineering Research Laboratory (CERL), and undergraduate students A. Gibson, D. Harmon, M. Sadowski and D. Jeffries at the University of Illinois.

REFERENCES

Bai, K. & Katz, J. 2014 On the refractive index of sodium iodide solutions for index matching in piv. *Exp. Fluids* **55**, 1–6.

Blois, G., Christensen, K. T., Best, J. L., Elliott, G., Austin, J., Dutton, C., Bragg, M., Garcia, M. & Fouke, B. 2012 A versatile refractive-index-matched flow facility for studies of complex flow systems across scientific disciplines. In *50th American Institute of Aeronautics and Astronautics (AIAA) Aerospace Sciences Meeting, Nashville, TN, AIAA*, *AIAA* 2012-0736, doi:10.2514/6.2012-736.

Calderon, D. E., Wang, Z., Gursul, I. & Visbal, M. R. 2013 Volumetric measurements and simulations of the vortex structures generated by low aspect ratio plunging wings. *Phys. Fluids* **25** (6), 067102.

CAMBONIE, T., GAUTIER, N. & AIDER, J.-L. 2013 Experimental study of counter-rotating vortex pair trajectories induced by a round jet in cross-flow at low velocity ratios. *Exp. Fluids* **54** (3), 1–13.

CHAMORRO, L. P., TROOLIN, D. R., LEE, S., ARNDT, R. E. A. & SOTIROPOULOS, F. 2013 Three-dimensional flow visualization in the wake of a miniature axial-flow hydrokinetic turbine. *Exp. Fluids* **54** (2), 1–12.

CHENG, B., SANE, S. P., BARBERA, G., TROOLIN, D. R., STRAND, T. & DENG, X. 2013 Three-dimensional flow visualization and vorticity dynamics in revolving wings. *Exp. Fluids* **54** (1), 1–12.

CHUA, L., YU, S. & WANG, X. 2003 Flow visualization and measurements of a square jet with mixing tabs. *Exp. Therm. Fluid Sci.* **27** (6), 731–744.

DONG, S. & MENG, H. 2004 Flow past a trapezoidal tab. *J. Fluid. Mech.* **510**, 219–242.

ELAVARASAN, R. & MENG, H. 2000 Flow visualization study of role of coherent structures in a tab wake. *Fluid Dyn. Res.* **27** (3), 183–197.

GAD-ELHAK, M. 2000 *Flow Control: Passive, Active and Reactive Flow Management*. Cambridge University Press.

GHANEM, A., HABCHI, C., LEMENAND, T., DELLA VALLE, D. & PEERHOSSAINI, H. 2013 Energy efficiency in process industry – high-efficiency vortex (HEV) multifunctional heat exchanger. *J. Renew. Energy* **56**, 96–104.

GHANEM, A., LEMENAND, T., DELLA VALLE, D., HABCHI, C. & PEERHOSSAINI, H. 2012 Vortically enhanced heat transfer and mixing: state of the art and recent results. In *ASME 2012 Heat Transfer Summer Conference*, pp. 21–30. American Society of Mechanical Engineers.

GRETTA, W. J. 1990 An exsperimental study of the fluid mixing effects and flow structure due to surface mounted passive vortex generating device. Master's thesis, Lehigh University, Bethlehem, PA, USA.

GRETTA, W. J. & SMITH, C. R. 1993 Flow structure and statistics of a passive mixing tab. *Trans. ASME* **115** (2), 255–263.

HABCHI, C., LEMENAND, T., DELLA VALLE, D. & PEERHOSSAINI, H. 2010*a* Alternating mixing tabs in multifunctional heat exchanger-reactor. *Chem. Engng Process.* **49** (7), 653–661.

HABCHI, C., LEMENAND, T., VALLE, D. & PEERHOSSAINI, H. 2010*b* Turbulence behavior of artificially generated vorticity. *J. Turbul.* **11** (36), 1–28.

HAMED, A. M., KAMDAR, A., CASTILLO, L. & CHAMORRO, L. P. 2015 Turbulent boundary layer over 2D and 3D large-scale wavy walls. *Phys. Fluids* **27** (10), 106601.

HUNT, J. C. R., WRAY, A. A. & MOIN, P. 1988 Eddies, streams, and convergence zones in turbulent flows. *Center for Turbulence Research Report CTR-S88*, p. 193.

JEONG, J. & HUSSAIN, F. 1995 On the identification of a vortex. *J. Fluid Mech.* **285**, 69–94.

KACI, H. M., HABCHI, C., LEMENAND, T., DELLA VALLE, D. & PEERHOSSAINI, H. 2010 Flow structure and heat transfer induced by embedded vorticity. *Intl J. Heat Mass Transfer* **53** (17), 3575–3584.

LÖGDBERG, O., FRANSSON, J. H. M. & ALFREDSSON, P. H. 2009 Streamwise evolution of longitudinal vortices in a turbulent boundary layer. *J. Fluid Mech.* **623**, 27–58.

MORICONI, L. 2009 Minimalist turbulent boundary layer model. *Phys. Rev.* E **79** (4), 046306.

PARK, J., PAGAN-VAZQUEZ, A., ALVARADO, J. L., CHAMORRO, L. P., LUX, S. & MARSH, C. 2016 Experimental and numerical visualization of counter rotating vortices. *J. Heat Transfer* **138** (8), 080908.

PEREIRA, F. & GHARIB, M. 2002 Defocusing digital particle image velocimetry and the three-dimensional characterization of two-phase flows. *Meas. Sci. Tech.* **13**, 683–694.

PEREIRA, F., GHARIB, M., DABIRI, D. & MODARRESS, D. 2000 Defocusing digital particle image velocimetry: a 3-component 3-dimensional DPIV measurement technique. Application to bubbly flows. *Exp. Fluids* **29**, S078–S084.

REEDER, M. & SAMIMY, M. 1996 The evolution of a jet with vortex-generating tabs: real-time visualization and quantitative measurements. *J. Fluid Mech.* **311**, 73–118.

SHARP, K., HILL, D., TROOLIN, D., WALTERS, G. & LAI, W. 2010 Volumetric 3-component velocimetry measurements of the turbulent flow around a Rushton turbine. *Exp. Fluids* **48** (1), 167–183.

STEPHENS, A. V. & COLLINS, G. A. 1955 Turbulent boundary layer control by ramps or wedges. *Australian Aeronautical Research Committee – Report* p. 19.

SUN, Z., SCHRIJER, F. F. J., SCARANO, F. & VAN OUDHEUSDEN, B. W. 2012 The three-dimensional flow organization past a micro-ramp in a supersonic boundary layer. *Phys. Fluids* **24** (5), 055105.

TROOLIN, D. & LONGMIRE, E. K. 2009 Volumetric velocity measurements of vortex rings from inclined exits. *Exp. Fluids* **48** (3), 409–420.

WU, Y. & CHRISTENSEN, K. T. 2006 Population trends of spanwise vortices in wall turbulence. *J. Fluid Mech.* **568** (1), 55–76.

YANG, W., MENG, H. & SHENG, J. 2001 Dynamics of hairpin vortices generated by a mixing tab in a channel flow. *Exp. Fluids* **30** (6), 705–722.

YE, Q., SCHRIJER, F. F. J. & SCARANO, F. 2016 Boundary layer transition mechanisms behind a micro-ramp. *J. Fluid Mech.* **793**, 132–161.

YU, Y., ZHANG, J. & SHAN, Y. 2015 Convective heat transfer of a row of air jets impingement excited by triangular tabs in a confined crossflow channel. *Intl J. Heat Mass Transfer* **80**, 126–138.

ZAMAN, K., REEDER, M. & SAMIMY, M. 1994 Control of an axisymmetric jet using vortex generators. *Phys. Fluids* **6** (2), 778–793.

ZHOU, J., ADRIAN, R. J., BALACHANDAR, S. & KENDALL, T. M. 1999 Mechanisms for generating coherent packets of hairpin vortices in channel flow. *J. Fluid Mech.* **387**, 353–396.